Nanoscale

Accepted Manuscript

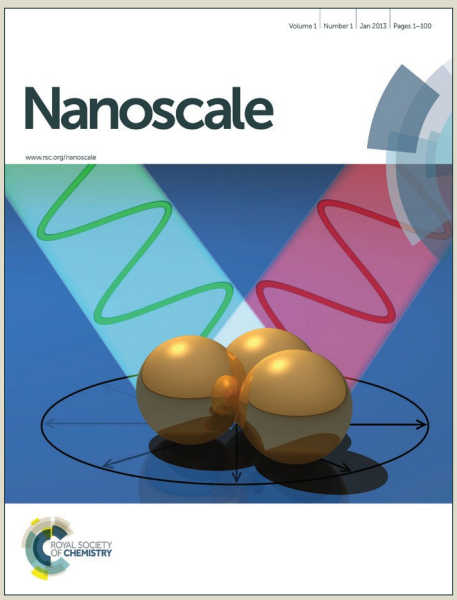

ROYAL SOCIETY OF CHEMISTRY

www.rsc.org/nanoscale

Tunneling Holes in Microparticles to Facilitate the Transport of Lithium Ions for High Volumetric Density Batteries

*Jian Zhu, K. Y. Simon Ng, Da Deng**

Department of Chemical Engineering and Materials Science, Wayne State University, 5050 Anthony Wayne Dr., Detroit, Michigan, United States, 48202

TOC

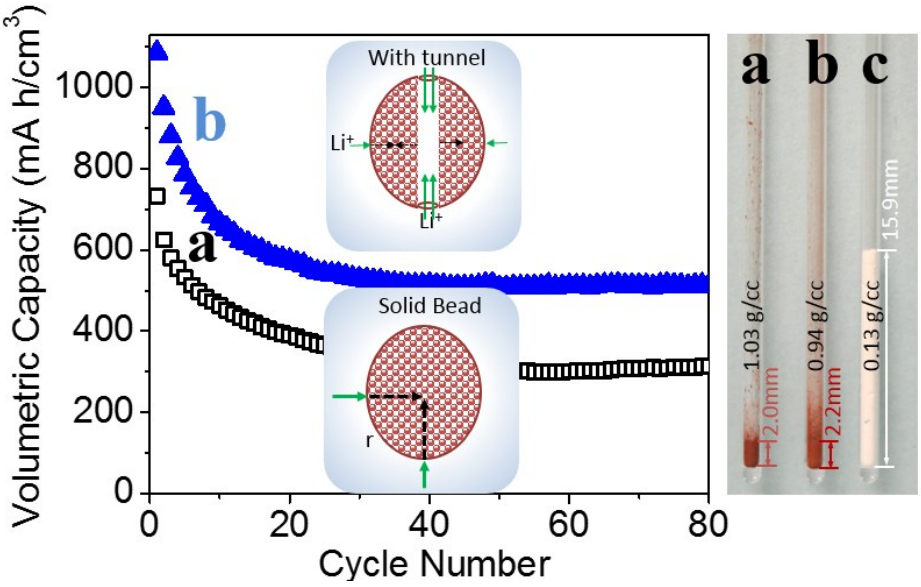

We tried to address the low accessibility issue of microparticles, which have desirable high volumetric capacity (mA·h/cm^3) than that of nanoparticles, by tunneling holes in those microparticles, achieving dramatically improved results.

KEYWORDS: microparticle, nanotunnel, lithium ion storage, volumetric capacity, transport.

ABSTRACT. Microscale materials generally have higher tap density than that of random nanoparticles. Therefore, microparticles have been attracting much attention for application as high volumetric density electrodes for lithium ion batteries. However, microparticles have much longer electrolyte diffusion and Li-ion migration length and less accessibility to electrolyte than that of nanoparticles. Therefore, it will be interesting to tunnel holes in the high volumetric density microparticles to facilitate the reversible storage of lithium ions. Here, tunnel-like holes were generated in microparticles to dramatically increase the accessibility of the active materials to facilitate the lithium ion transfer. A plausible formation mechanism to explain the generation of tunnel-like was proposed based on time-course experiments and intensive characterization. Impressively, the as-prepared microbeads with tunnels demonstrated dramatically improved performance as compared to the solid microbeads without tunnels in lithium ion storage. The microparticles with tunnels could achieve comparable electrochemical performances to those nanoparticles reported in literature, suggesting microparticles, properly tuned, could be promising candidates as negative electrode for lithium-ion batteries and worthy further studies. We also directly measured the volumetric density of the microparticles. We would like to highlight that superior volumetric capacity of 514 mA h/cm^3 has been achieved. We hope to promote more frequent use of unite of mA h/cm^3 in addition to the conventional unit of mA h/g in the battery community.

1. Introduction

Microstructured materials formed by the aggregation of nanoparticles as building units for lithium-ion batteries (LIBs) have been attracting much attention recently. Microstructured

materials of nanoparticle aggregates offer a number of notable advantages as compared to that of random nanoparticles, generally: (1) microstructures have higher tap density, (2) microstructures have reduced inter-particle resistance, (3) microstructures have reduced surface induced side reactions, (4) microstructures have lower electrode–electrolyte contact area or less irreversible capacity loss associated with SEI formation, as compared to that of random nanoparticles. Meanwhile, the gaps or pores between nanoscale building units will facilitate the electrolyte and ion transfer. For example, microsized ensemble of Si@void@carbon nanoparticles demonstrated superior cyclability of 97% capacity retention after 1,000 cycles due to the hierarchical arrangement of nanoparticles.[1] Micro-nano hierarchical structured $LiFePO_4$/C composites showed both excellent rate performance and high tap density as the positive electrode for LIBs.[2] Multishelled TiO_2 hollow microsphere has achieved superior cyclability at 10C for 1,200 cycles.[3] Microstructured Fe_2O_3 with improved electrochemical performance as compared to random nanoparticles have been demonstrated to address the issue of low volumetric energy density of Fe_2O_3 nanoparticles.[4] $Li_4Ti_5O_{12}$ microsphere with size ~10-20 μm formed by aggregated carbon-coated nanoparticles demonstrated improved rate performance due to enhanced conductivity and improved intercalation kinetics from its unique structure. Meanwhile, the microsized spheres also have an impressive high tap density of 0.82 g/cm^3.[5]

Microstructured materials can find important applications, including energy storage,[5-8] catalyst,[9-11] sensor,[12,13] carriers in medical application,[14] etc. For example, multi-shelled hollow microspheres of α-Fe_2O_3 ,Co3O4, and SnO_2 microbox have been used as negative electrode materials for LIBs achieving superior performances.[7,8] Au@TiO_2 core-shell hollow spheres,[15] multishelled ZnO hollow microspheres,[16] quintuple-shelled SnO_2 hollow microspheres,[17] have been reported for high performance dye-sensitized solar cells. Multi-shelled Mn_2O_3 hollow

microspheres were prepared for high-performance supercapacitors.[18] Multi-shell Au/CeO_2 has demonstrated improved catalytic performance in the reduction of p-nitrophenolas.[19] Microspheres of $(ZnS)_x(CuInS_2)_{1-x}$, as photocatalysts with tunable band gap, have demonstrated excellent performances in water splitting.[10] Microspheres of ZnO have demonstrated impressive sensitivity in gas sensor application.[13] Hollow microspheres of polymers have been applied as injectable cell carriers for knee repair.[14] Both template-free and template-assisted approaches have been explored to create holes or hollow voids in microstructures.[20] Template-assisted synthesis is based on the use of sacrificed soft and hard templates.[21,22] Template-free synthesis is developed based various mechanisms of formation, such as Kirkendall effect,[23] Ostwald ripening process,[24,25] etching treatment,[8,9,26], and self-template fabrication.[27,28] Template-free synthesis is highly desirable in many cases where suitable templates are not easily available. However, template-free synthesis is not as predictable as those by template-assisted synthesis. Therefore, it will be interesting to carve holes in microparticles from non-hollow microparticles to preserve the predictable microscale morphologies and achieve the advantages of hollow structures.

Here, we demonstrate that it is possible to carve tunnel-like holes in hematite microparticles forming chevron bead-like morphology for high volumetric capacity negative electrodes in LIBs. The plausible formation mechanisms involved was revealed by extensive characterizations. Experimentally evidenced, both Ostwald ripening mechanism and ionic etching process are involved in carving the unique tunnel-like holes in microparticles. The chevron bead-like structure can provide higher surface to volume ratio, shorter transport lengths, higher permeability, as compared to solid microparticles. At the same time, the unique structure could have a relatively higher bulk density than that of highly hollow structures, which is favorable in many fields of applications, such as energy storage devices where tap density matters. In LIBs,

the electrolyte or lithium ions can easily reach the core part of the microstructures via the tunnels/holes and the diffusion distance of electrolyte and migration length of lithium ions in the microstructures with tunnel-like holes decreased to *r/2*, as compared to long diffusion distance of *r* in similar solid microparticles. The schematic of the comparison of solid microstructures and microstructures with tunnel-like holes in LIB application is illustrated in Figure 1. The tunnels can theoretically increase the contact area between solid active materials and liquid electrolyte and the length of electrolyte transfer from outside to the deepest part in mirostructure is greatly decreased. Additionally, the tunnel-like holes can effectively accommodate the stress caused by the volume variation during the repeating lithium insertion/extraction processes. In other words, the microparticles with tunnel-like holes could offer the advantages of both high volumetric density and cyclablity. The chevron bead-like hematite microstructures have a high tap density of 0.94 g/cm^3, which is significantly higher than that of commercial P25 TiO_2 nanoparticles at 0.13 g/cm^3 only, or more than sevenfold increase. When tested as the electrode material for LIBs, the chevron bead like microparticles demonstrated improved electrochemical performances in terms of specific capacity, volumetric capacity, Coulombic efficiency, and cyclability as compared to that of solid beads.

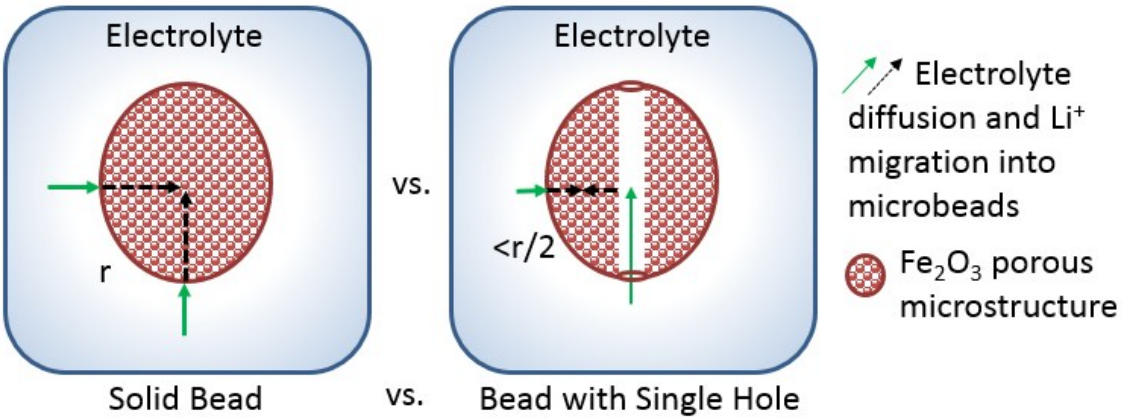

Figure 1. Schematic to illustrate the shorter distance of electrolyte diffusion/Li^+ migration in microstructure with tunnel-like hole (right) as compared to that of solid microstructure (left).

2. Experimental Section

Materials Preparation. Typically, 0.4 mmol of $FeCl_3.6H_2O$ and 0.1 mmol of D-glucose were dissolved in 16 ml of DI-water (solution A), and 0.25 mmol of dimethyl oxalate (DMO) was dissolved in 16 ml of 1-propanol (solution B). Solution A was added into solution B drop-wisely under stirring, and the mixture was stirred for 15 min. The mixture was then transferred into a 50 ml Teflon-lined autoclave and heated at 200 °C for 3 h. The solid product of *α-Fe_2O_3* microscale chevron beads in red color was washed repeatedly with water and ethanol, collected by centrifugation and dried in a vacuum oven overnight.

Materials Characterization. Powder X-ray diffraction (XRD) was carried out with a Rigaku Smartlab X-ray diffractometer using Cu Kα radiation. Energy-dispersive X-ray spectroscopy (EDS) and morphology characterization were carried out on a field emission scanning electron microscopy (FESEM, JSM-7600, equipped with Pegasus Apex 2 integrated EDS) with accelerating voltage of 15 kV. TEM images were taken by transmission electron microscopy (TEM, JEOL 2010) with operating voltage of 200 kV. Measurement of Brunauer–Emmett–Teller (BET) surface areas and pore size distribution were carried out using N_2 adsorption/desorption isotherms surface area analyzers (Tristar II 3020)

Electrochemical Measurement. The as-prepared α-Fe_2O_3 chevron microbeads were mixed with carbon black (Super C65 from TIMCAL), and polyvinylidene fluoride (PVDF) at weight ratio of 8:1:1 in a N-methylpyrrolidone (NMP) solvent to prepare the slurry. The slurry was then applied to copper discs as current collectors and dried at 100 ^oC overnight. Electrochemical cells were assembled in an argon-filled glove box using 1 M solution of $LiPF_6$ in ethylene carbonate (EC) and diethyl carbonate (DEC) (1:1, v/v) as the electrolyte, PP/PE/PP trilayer membrane (Celgard 2320) as the separator, metallic lithium foil as counter and reference electrodes. The cells were

tested galvanostatically at current of 200mA/g at room temperature in a voltage window of 0.05V-3V on a MTI BST8-WA battery tester.

3. Result and Discussion

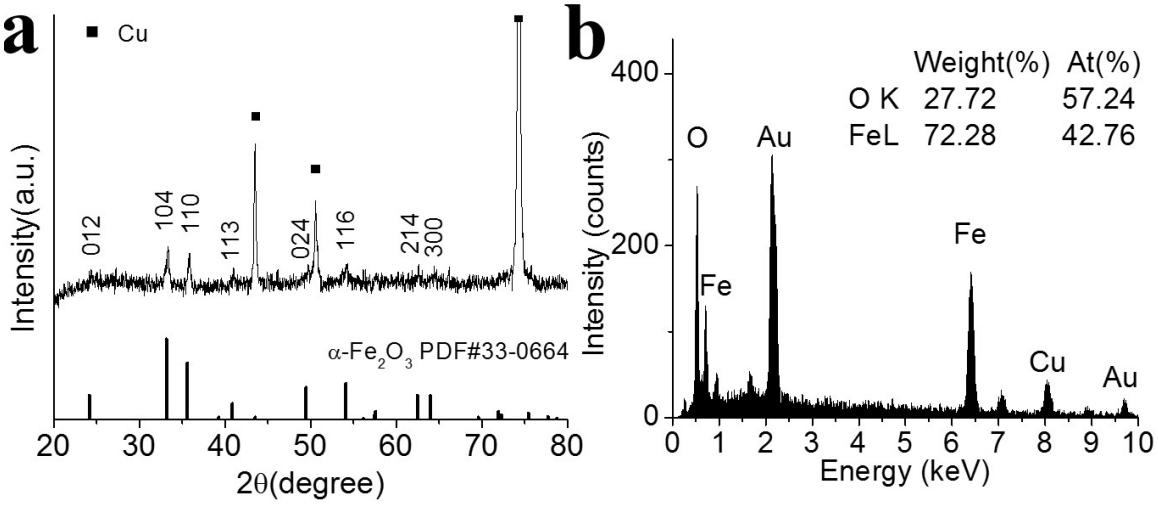

Figure 2. (a) XRD pattern of as-prepared α-Fe_2O_3 chevron microbeads. Peaks of Cu come from the Cu disc substrate. (b) EDS of as-prepared α-Fe_2O_3 chevron microbeads showing the atomic ratio of Fe to O at ~2:3. Peaks of Au come from sputter coating of Au and Cu peaks are from the substrate.

The chemical composition of as-prepared material was characterized by XRD and EDS (Figure 2). All the XRD peaks can be assigned to α-Fe_2O_3 (Figure 2a). The dominant copper peaks are from the sample holder. The peaks located at ~24°, 33°, 36°, 41°, 49°, 54°, 62°, and 63° are typical diffractions from α-Fe_2O_3 (JCPDS card no. 33-0664). The XRD analysis indicates the pure α phase of Fe_2O_3 was synthesized via the solvothermal method. The crystalline size calculated based on Scherrer Equation from strongest (104) peak of α-Fe_2O_3 is 19 nm. The chemical composition of the as-prepared α-Fe_2O_3 was double-confirmed by the EDS spectrum (Figure 2b). The atomic ratio of Fe:O is ~ 2:3, which is in consistent with Fe_2O_3.

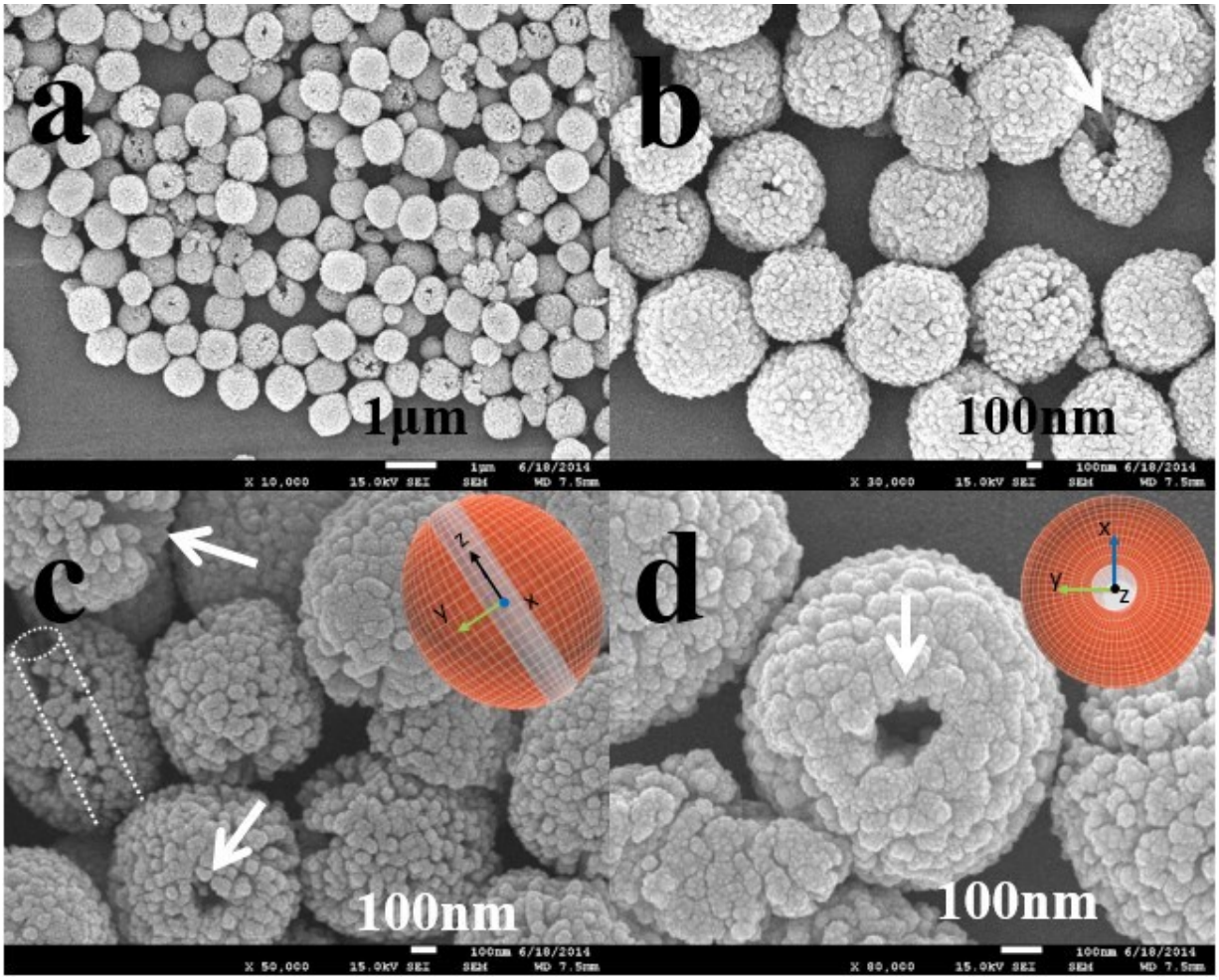

Figure 3. FESEM images for typical α-Fe_2O_3 chevron microbeads with tunnel-like holes each at different magnifications: (a) overview of α-Fe_2O_3 microscale hole beads; (b) high magnification view of a few representative hole beads; the white arrow highlights the microbead with one end of tunnel broken; and (c) one microbead with broken shell suggests that the hole penetrates the core of the microbead forming a tunnel (marked by dash line); and (d) top view of a single hole bead clearly showing the rough surface inside and outside; insets of (c) and (d) are the 3D illustrations of the hole bead to easily interpret the direction of views of those corresponding FESEM images of microsize hole beads.

The morphology of α-Fe_2O_3 microbeads was revealed by FESEM (Figure 3). The low-magnification FESEM image (Figure 3a) shows the overall size distribution of the α-Fe_2O_3 microbeads and each bead is at about 700 nm in length and 600 nm in width, all in chevron bead-like shape. Figure 3b clearly shows the open endings/holes on the microbead, highlighted by the white arrow. The holes are on the two ends of the long axis. A FESEM image with higher magnification (Figure 3c) shows the tunnel-like holes in the microbeads (indicated by white arrows). A side-view of a microbead with the shell partially broken (highlighted by dash line) indicates that the tunnel connects the two ends through the microbead. A high-magnification FESEM image of the top view of a single chevron microbead is shown in Figure 3d. The rough surface inside and outside of the microbeads suggests that the microbeads were constructed by aggregation of nanoparticles/gains as the basic building units. The size of the building units is around 20-30 nm, which is in consistent with the size calculated by Scherrer Equation based on XRD. To better interpret the morphology observed by FESEM, the 3D model of this microstructure was drawn. The insets in Figure 3c, d are the 3D model of the corresponding microbeads which could help to visualize the chevron microbeads viewed from different perspectives.

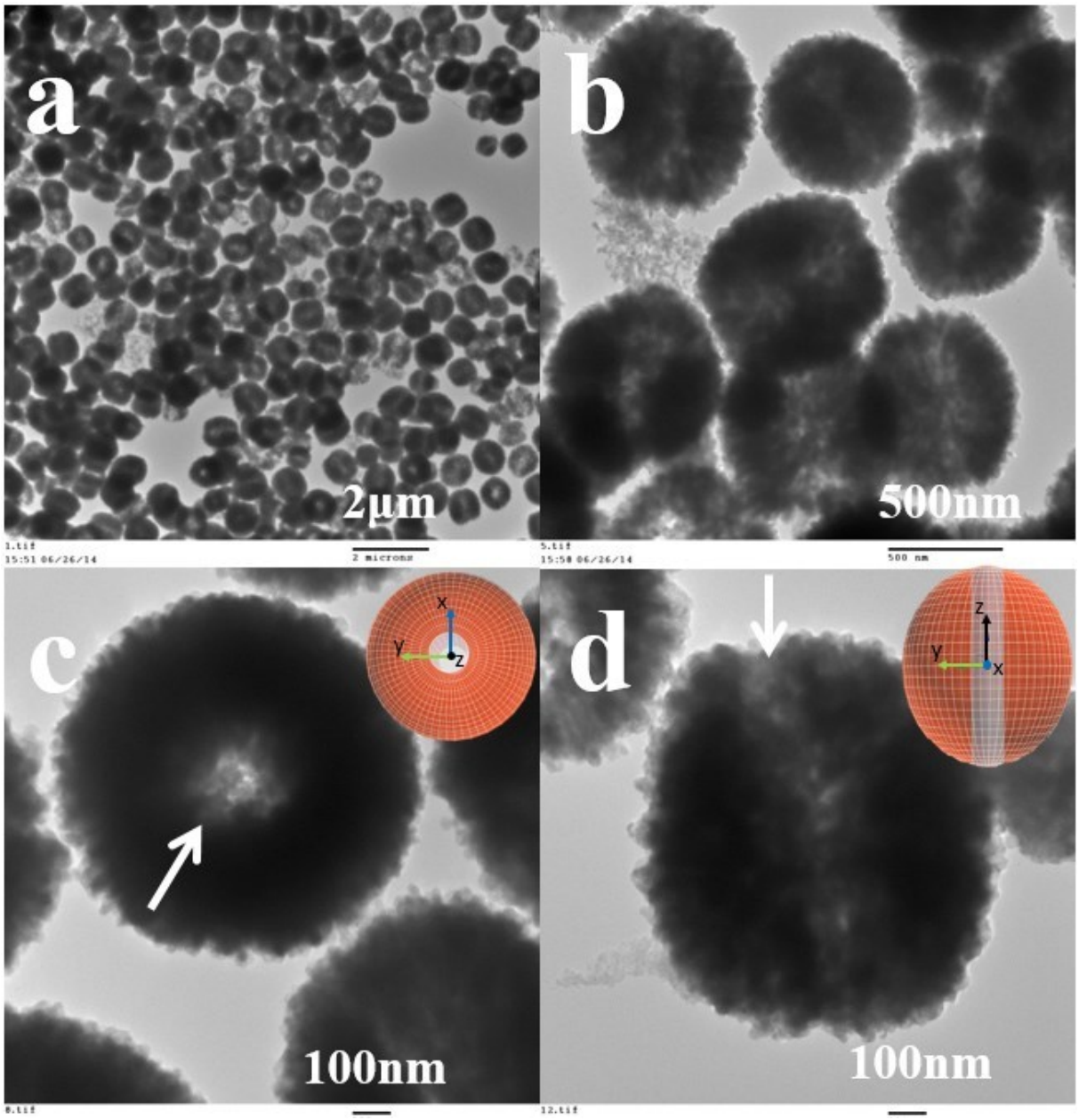

Figure 4. TEM images of α-Fe_2O_3 chevron microbeads: (a) low-magnification view and (b) high-magnification view; (c) top view and (d) side view of representative microbeads to clearly reveal the tunnel-like holes. The tunnel-like holes are marked by white arrows. Insets are the corresponding 3D model to better interpret those TEM images.

The unique chevron bead-like structure was further revealed by TEM (Figure 4). The overall view of the microbeads with a light contrast line in each bead reveals the tunnel-like holes in all

microbeads (Figure 4a). The high-magnification TEM image of a few representative hole beads more clearly shows the tunnels alight along the longest axis of the microbeads (Figure 4b). The top view and the side view of representative single microscale chevron bead are shown in Figure 4c and Figure 4d, respectively. The observation of ring-like TEM color contrast with a tiny hole in Figure 4c suggests the projection is along the tunnel or top view. The observation of light contrast line inside the microbead more clearly shows the tunnel and the projection is perpendicular to the tunnel or side view (Figure 4d). The 3D models are provided as the insets of Figure 4c and Figure 4d to illustrate the corresponding microbeads viewed from different perspectives under TEM. The surface area and pore size distribution of solid beads and beads with tunnel obtained were investigated BET analysis based on N_2 adsorption–desorption at 77 K (Figure S2 in SI). The BET surface areas of solid and hole-beads were 23.6 m^2/g and 16.0 m^2/g, respectively. It is interesting to note that the solid beads have higher surface area than that of hole beads. This observation could be rationalized. Both beads were formed by aggregation of nanoparticles as building units. The beads with tunnel-like holes were formed after 3 h of reaction where the nanoparticle building units have size about ~ 20-30 nm. In contrast, the solid beads were formed after 1 h of reaction where the building units have significantly small size about ~5-10 nm (Figure S1c-d in supporting information). Although tunnel-like holes were formed after 3 h, the total surface area actually decreased due to the fact that the holes generated were not enough to compensate the area creased due to crystalline growth. The pore size distributions obtained by BJH method of both samples are similar: the pore size mainly centered around 9 nm. The pore diameter of 9 nm may be attributed to the void space between nanoparticle building unit aggregates.

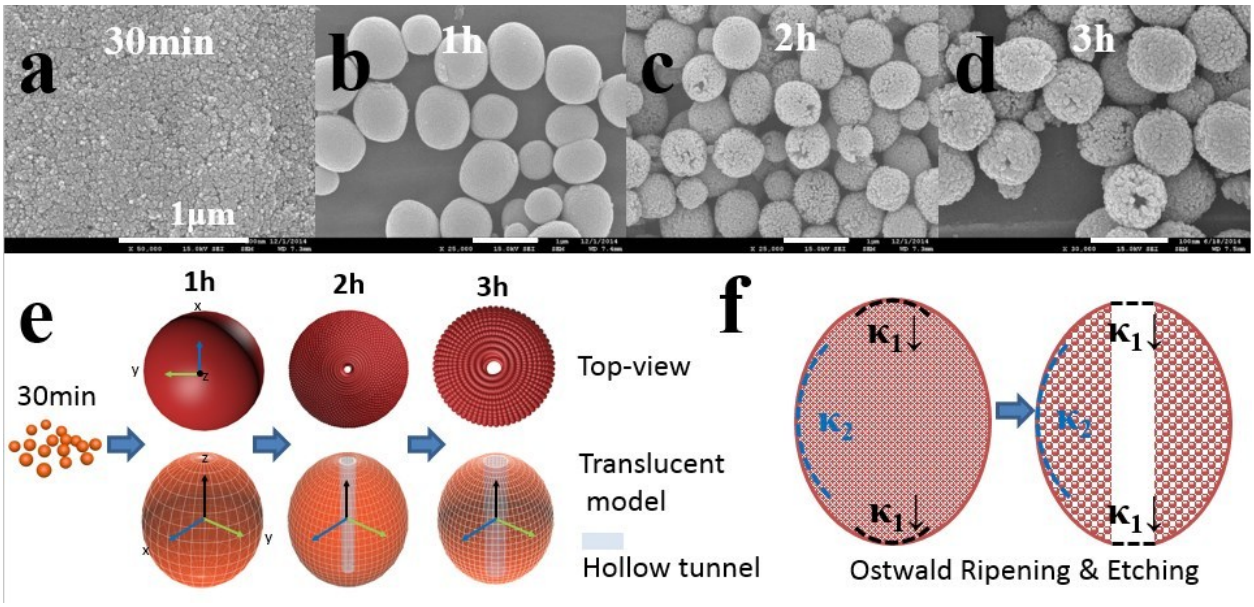

Figure 5. (a-d) *Ex-situ* FESEM characterization of particles obtained after different time of reaction to show the structural evolution: (a) 30 min; (b) 1 h; (c) 2 h; (d) 3 h. The scale bars of all FESEM images are 1 μm. (e) Illustrations of steps of structural evolution involved in the formation of micro chevron beads from time-course experiments of (a-d). (f) Illustration of formation of tunnel through Ostwald ripening process and ion assisted etching process at locations of high curvature (κ_1), leading to fast dissolving process at those locations and formation of tunnel-like hole.

To understand the mechanism of the formation of the unique chevron microbeads, a set of time-course experiments, from 30 min to 3 h, were carried out. The structural evolution was revealed by *ex-situ* FESEM characterization (Figure 5 a-d). At the early stage of reaction after 30 min, nanoparticles formed by nucleation and precipitation (Figure 5a). The as-formed nanoparticles were brown in color (optical image, Figure S1a in SI), indicating intermediates or the precursors formed at this stage. At the second stage after 1 h, nanoparticles aggregated and formed solid microbead in ellipsoid shape with smooth surface (Figure 5b). The aggregation and

growth may be ascribed as the oxalate ions released by dimethyl oxalate which could guide the oriented attachment due to the ability of oxalate anions, as a binary ligand, to bind with two metallic cations.[24] The optical image (Figure S1b in SI) shows the change of color from brown to red with reaction time increases from 30 min to 1h, indicating the conversion of the nanoparticles intermediate to α-Fe_2O_3 with typical red color. At the third stage after 2 h, the overall chevron bead-like microstructure started to form (Figure 5c). The locations with higher surface energy or smaller building units, are more vulnerable to be etched and dissolved. At the same time, the location with less surface energy or larger building units, continue to grow. The microbeads become porous due to the aggregation of larger building units. At the final stage after 3 h, the final α-Fe_2O_3 product with distinguishable tunnel formed. The plausible mechanism for the formation of tunnel-like hole is proposed based on our experimental observation and illustrated in Figure 5f. Based on Ostwald ripening mechanism, small nanoparticles building units, distributed mainly at locations with large curvature or higher surface energy, are easily dissolved and re-precipitate on to big nanoparticles, to minimize energy.[29,30] Additionally, the Cl^- assisted H^+ etching may also contribute to the formation tunnel-like holes. The anion-assisted etching of metal oxide, like Cl^-, $[SO_4]^{2-}$ and $[VO_4]^{3-}$ assisted, or $[H_2PO_4]^-$ assisted etching of Fe_2O_3, F^- assisted etching of TiO_2, have been reported where the etching only occurred at selective locations to create unique structures.[9,31-33]

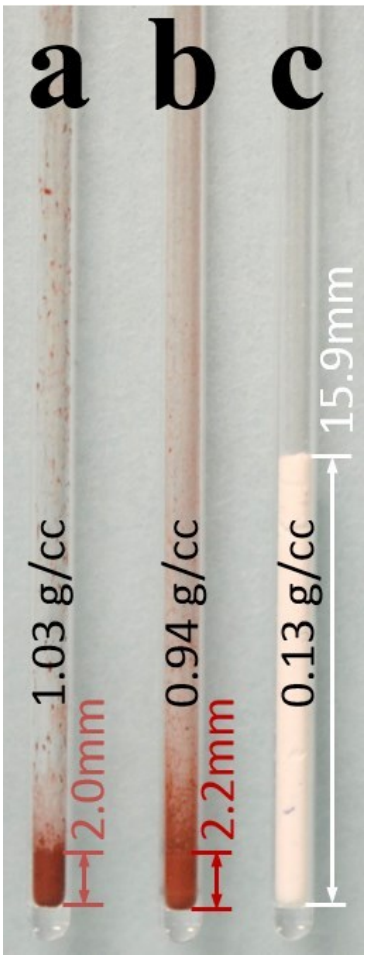

Figure 6. Optical image to show different tap densities of (a) solid microbead and (b) chevron microbead of α-Fe_2O_3 with tunnels, (c) commercial TiO_2 nanoparticles (AEROXIDE, P25), in glass tubes with height of 2.0mm, 2.2mm and 15.9 mm, respectively. The tap densities are estimated to be 1.03 g/cm^3, 0.94 g/cm^3 and 0.13g/ cm^3 for solid microbeads, chevron microbeads with tunnels and TiO_2 nanoparticles, respectively.

In order evaluate the volumetric capacity (mA h/cm^3), in additional that of specific capacity (gravimetric capacity mA h/g) dominantly used in battery research, the tap densities of the as-prepared beads with and without tunnels were measured. The tap densities of as-prepared α-Fe_2O_3 solid microbeads and chevron microbeads with tunnels are much higher than that of a common commercial nanomaterial, TiO_2 nanoparticles (AEROXIDE TiO_2 P25) (Figure 6). The

solid microbeads were obtained following the same typical synthesis procedure outlined in experimental section, but with only 1h reaction instead of 3 h (Figure 5b). All the materials with the same weight were put into glass tubes with one end open and their heights were measured. The tap densities of micro solid beads and micro chevron beads were estimated to be 1.03 g/cm^3 and 0.94 g/cm^3, respectively, using the tap density of commercial P25 at 0.13 g/cm^3 as the reference.[26] We used P25 TiO_2 nanoparticles here as commercial α-Fe_2O_3 with known tap density was not easily accessible to us. On the other hand, P25 TiO_2 has known tap density and widely used as control in various studies. The much higher tap densities of both solid beads and beads with tunnels as compared to that of TiO_2 nanoparticles can be attributed to their microscale structures. As compared to the solid microbeads, chevron microbeads with tunnels have slightly lower tap density due to the presence of nanotunnels in beads. The high tap density enables the application of α-Fe_2O_3 microbeads as promising high volumetric capacity negative electrode materials.

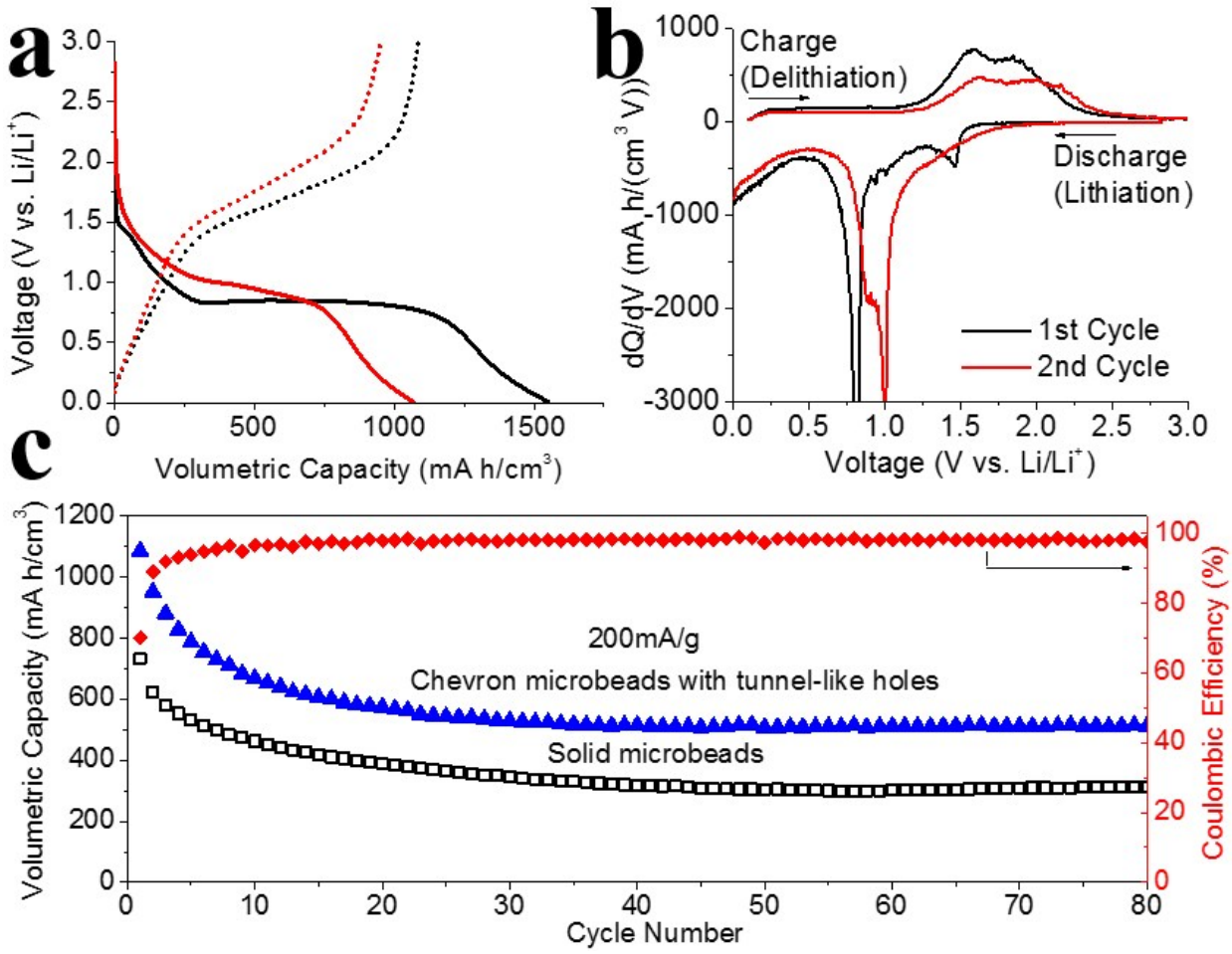

Figure 7. Electrochemical performance of α-Fe_2O_3 micro chevron beads with tunnel-like holes: (a) charge-discharge profiles of the first two cycles; (b) dQ/dV vs. V plot for the first two cycles; and (c) cycling performance of the microbeads with tunnels (blue triangles) as compared to solid microbeads for 80 cycles (black squares) in terms of volumetric capacity (mAh/cm^3).

The as-prepared α-Fe_2O_3 micro chevron beads with tunnel-like holes and α-Fe_2O_3 solid microbeads were preliminarily tested as negative electrode materials for LIBs (Figure 7). We would like to highlight that we used volumetric capacity (mAh/cm^3) in our plots. The volumetric capacity was converted from specific capacity (Figure S3 in supporting information) based on the tap density established (Figure 6). The charge-discharge profiles and differential capacity (dQ/dV) vs. voltage plots for the first two cycles are shown in Figure 7a and Figure 7b,

respectively. The first cycle discharge capacity is 1549 mA h/cm^3 (1648 mAh/g). The volumetric energy storage density estimated is ~1400 Wh/L, based on pure anode materials in the Li-metal testing cell. A small slope starts at around 1.5 V and ends at around 0.8 V followed by a plateau at around 0.8 V (Figure 7a). It can be attributed to the lithium intercalation into Fe_2O_3 and then the reduction of Fe^{3+} to Fe^0 and formation of solid-electrolyte interface (SEI), respectively.[34] The much higher specific capacity of the first cycle than theoretical value (1007 mAh/g) and the first cycle irreversible capacity loss of ~479 mA h/cm^3 (510 mAh/g, 31%) may be attributed to the formation of SEI and decomposition of electrolyte in the first cycle.[7,35] To better interpret the electrochemical reactions involved, the dQ/dV vs. V plot was analyzed (Figure 7b). A weak peak at ~1.5 V and a strong peak at ~0.8 V are observed in the first discharge profile, which can be assigned to intercalation of Li^+ and reduction of iron ion to metallic iron and the formation of SEI, respectively.[7,24,34,36] In the 2nd cycle, only one discharge peak can be observed and it shifted to ~1.0 V.[7,35] This shift of peak is associated with drastic, lithium-driven, structural or textural modifications.[37,38] This peak gradually and slightly shifted from 1.0 back to 0.7 V from the 2nd cycle to the last cycle (80th cycle, dQ/dV in Figure S4 in Supporting Information). In the charging process, a broad peak between 1.5-2.0 V can be observed, which can be attributed to delithiation reaction, corresponding to the oxidation of Fe^0 back to Fe^{3+}.[39] The cycling performance in terms of volumetric capacity of chevron microbeads is shown in Figure 7c. The sample was tested at current of 200 mA/g for 80 cycles. The capacity fades in the first twenty cycles, remains at around 514 mA h/cm^3 for 60 more cycles.

The experimental results also confirmed that electrochemical performances can be enhanced by carving holes/tunnels in microscale particles from solid microparticles. The comparison of charge-discharge curves and dQ/dV plots indicates that same electrochemical reactions were

involved for both samples from the 1st cycle to the last cycle (Figure S3a-d in SI). The cycling performance of the solid microbeads for 80 cycles was analyzed (Figure 6c and Figure S3e in SI), as compared to the chevron microbeads with tunnel-like holes. The chevron microbeads with tunnels possess higher discharge capacity in terms of both specific capacity and volumetric capacity than that of solid microbeads. Although the tap density of solid bead is slightly higher than that of beads with tunnels, the much higher specific capacity of the later still warrant that the volumetric density of beads with tunnels is higher than that of solid beads. The surface area of chevron microbeads with tunnel-like holes is less than that of solid microbeads, and both samples have similar pore size distribution. So the improved electrochemical performance can be attributed to the advantages provided by the carved holes in microparticles: (1) decreased distance of for electrolyte diffusion and Li-ion migration from outside to the inside of the microbead structure; (2) alleviated stress caused by the volume variation during the repeating lithium insertion/extraction processes. The are many different parameters that could affect the electrochemical performances of the materials, including conductivity, morphology and size. Our results show that the void space may positively impact the electrochemical performance, even though the crystalline size increased. However, further studies are still required to gain better understanding. The charge-discharge curves and dQ/dV plot of α-Fe_2O_3 solid microbeads as compared to those of α-Fe_2O_3 chevron microbeads are shown in Figure S3 in the supporting information. The positions of all the discharge/charge peaks of solid microbeads are almost identical to those of chevron microbeads with holes, indicating the same electrochemical reactions involved.[40,41] The practical specific capacity (by mass) of as-prepared α-Fe_2O_3 microbeads (545 mAh/g) is in the same order of scale as commercial P25 TiO_2 (168 mA/g). However, the volumetric capacity density of the as-prepared α-Fe_2O_3 micro chevron beads is 519

mA h/cm^3, is 50% higher than 345 mA h/cm^3 of α-Fe_2O_3 solid microbeads, due to the much higher specific capacity as compared to those of solid microbeads. And it has a volumetric capacity 23 times higher than 22 mA h/cm^3 of P25 TiO_2. Therefore, the chevron microbeads could be promising as high tap density electrode materials for compact LIBs.

4. Conclusion

In summary, we have successfully prepared α-Fe_2O_3 micro chevron beads with tunnel-like holes by a facile and fast procedure. The formations mechanism was proposed based on experimental observations. When applied as negative electrode materials for LIBs, the unique micro chevron beads with tunnel-like holes exhibited a reasonably stable volumetric capacity at ~514 mA h/cm^3 for at least 80 cycles, which is superior as compared to the solid microbeads or those random nanoscale particles reported. As a result, the chevron bead-like hematite microstructure with high tap density and volumetric capacity will be promising negative electrode materials for high-energy density LIBs.

ASSOCIATED CONTENT

Supporting Information. Optical images, BET surface area and pore size distribution, electrochemical performance in terms of specific capacity and dQ/dV vs. V plot of the 80th cycle.

AUTHOR INFORMATION

Corresponding Author

Da Deng, E-mail: da.deng@wayne.edu

Author Contributions

D.D. designed the research. J.Z. conducted the experiments. K.Y.S.N. contributed to the discussions of results. D.D. and J.Z. wrote the first draft of the manuscript and all authors participated in the manuscript revision.

ACKNOWLEDGMENT

The authors thank Stephanie Brock for access to BET instrument and the Lumigen Instrument Center for access to SEM and TEM instruments, Wayne State University, Detroit, MI.

References

(1) Liu, N.; Lu, Z.; Zhao, J.; McDowell, M. T.; Lee, H.-W.; Zhao, W.; Cui, Y. A Pomegranate-Inspired Nanoscale Design for Large-Volume-Change Lithium Battery Anodes. *Nat. Nano.* **2014**, *9*, 187-192.

(2) Wang, M.; Yang, Y.; Zhang, Y. Synthesis of Micro-Nano Hierarchical Structured LiFePO4/C Composite with Both Superior High-Rate Performance and High Tap Density. *Nanoscale* **2011**, *3*, 4434-4439.

(3) Ren, H.; Yu, R.; Wang, J.; Jin, Q.; Yang, M.; Mao, D.; Kisailus, D.; Zhao, H.; Wang, D. Multishelled TiO2 Hollow Microspheres as Anodes with Superior Reversible Capacity for Lithium Ion Batteries. *Nano Lett.* **2014**, *14*, 6679-6684.

(4) Zhang, J.; Sun, Y.; Yao, Y.; Huang, T.; Yu, A. Lysine-Assisted Hydrothermal Synthesis of Hierarchically Porous Fe2O3 Microspheres as Anode Materials for Lithium-Ion Batteries. *J. Power Sources* **2013**, *222*, 59-65.

(5) Zhu, G.-N.; Liu, H.-J.; Zhuang, J.-H.; Wang, C.-X.; Wang, Y.-G.; Xia, Y.-Y. Carbon-Coated Nano-Sized Li4Ti5O12 Nanoporous Micro-Sphere as Anode Material for High-Rate Lithium-Ion Batteries. *Energy Environ. Sci.* **2011**, *4*, 4016-4022.

(6) Oh, S.-M.; Hwang, J.-Y.; Yoon, C. S.; Lu, J.; Amine, K.; Belharouak, I.; Sun, Y.-K. High Electrochemical Performances of Microsphere C-TiO2 Anode for Sodium-Ion Battery. *ACS Appl. Mater. Interfaces* **2014**, *6*, 11295-11301.

(7) Xu, S.; Hessel, C. M.; Ren, H.; Yu, R.; Jin, Q.; Yang, M.; Zhao, H.; Wang, D. α-Fe2O3 Multi-Shelled Hollow Microspheres for Lithium Ion Battery Anodes with Superior Capacity and Charge Retention. *Energy Environ. Sci.* **2014**, *7*, 632-637.

(8) Zhang, L.; Wu, H. B.; Liu, B.; Lou, X. W. Formation of Porous SnO2 Microboxes via Selective Leaching for Highly Reversible Lithium Storage. *Energy Environ. Sci.* **2014**, *7*, 1013-1017.

(9) Pan, J. H.; Zhang, X.; Du, A. J.; Sun, D. D.; Leckie, J. O. Self-Etching Reconstruction of Hierarchically Mesoporous F-TiO2 Hollow Microspherical Photocatalyst for Concurrent Membrane Water Purifications. *J. Am. Chem. Soc.* **2008**, *130*, 11256-11257.

(10) Lin, Y.; Zhang, F.; Pan, D. A Facile Route to (ZnS)x(CuInS2)1-x Hierarchical Microspheres with Excellent Water-Splitting Ability. *J. Mater. Chem.* **2012**, *22*, 22619-22623.

(11) Chen, F.; Zai, J.; Xu, M.; Qian, X. 3D-Hierarchical Cu3SnS4 Flowerlike Microspheres: Controlled Synthesis, Formation Mechanism and Photocatalytic Activity for H2 Evolution from Water. *J. Mater. Chem. A* **2013**, *1*, 4316-4323.

(12) Li, Z.; Zhou, Y.; Song, J.; Yu, T.; Liu, J.; Zou, Z. Versatile Nanobead-Scaffolded N-SnO2 Mesoporous Microspheres: One-Step Synthesis and Superb Performance in Dye-Sensitized Solar Cell, Gas Sensor, and Photocatalytic Degradation of Dye. *J. Mater. Chem. A* **2013**, *1*, 524-531.

(13) Wang, L.; Lou, Z.; Fei, T.; Zhang, T. Zinc Oxide Core-Shell Hollow Microspheres with Multi-Shelled Architecture for Gas Sensor Applications. *J. Mater. Chem.* **2011**, *21*, 19331-19336.

(14) Liu, X.; Jin, X.; Ma, P. X. Nanofibrous Hollow Microspheres Self-Assembled from Star-Shaped Polymers as Injectable Cell Carriers for Knee Repair. *Nat. Mater.* **2011**, *10*, 398-406.

(15) Du, J.; Qi, J.; Wang, D.; Tang, Z. Facile synthesis of Au@TiO2 core-shell hollow spheres for dye-sensitized solar cells with remarkably improved efficiency. *Energy Environ. Sci.* **2012**, *5*, 6914-6918.

(16) Dong, Z.; Lai, X.; Halpert, J. E.; Yang, N.; Yi, L.; Zhai, J.; Wang, D.; Tang, Z.; Jiang, L. Accurate Control of Multishelled ZnO Hollow Microspheres for Dye-Sensitized Solar Cells with High Efficiency. *Adv. Mater.* **2012**, *24*, 1046-1049.

(17) Dong, Z.; Ren, H.; Hessel, C. M.; Wang, J.; Yu, R.; Jin, Q.; Yang, M.; Hu, Z.; Chen, Y.; Tang, Z.; Zhao, H.; Wang, D. Quintuple-Shelled SnO2 Hollow Microspheres with Superior Light Scattering for High-Performance Dye-Sensitized Solar Cells. *Adv. Mater.* **2014**, *26*, 905-909.

(18) Wang, J.; Tang, H.; Ren, H.; Yu, R.; Qi, J.; Mao, D.; Zhao, H.; Wang, D. pH-Regulated Synthesis of Multi-Shelled Manganese Oxide Hollow Microspheres as Supercapacitor Electrodes Using Carbonaceous Microspheres as Templates. *Advanced Science* **2014**, *1*, DOI: 10.1002/advs.201400011.

(19) Xu, P.; Yu, R.; Ren, H.; Zong, L.; Chen, J.; Xing, X. Hierarchical nanoscale multi-shell Au/CeO2 hollow spheres. *Chemical Science* **2014**, *5*, 4221-4226.

(20) Lai, X.; Halpert, J. E.; Wang, D. Recent advances in micro-/nano-structured hollow spheres for energy applications: From simple to complex systems. *Energy Environ. Sci.* **2012**, *5*, 5604-5618.

(21) Wang, B.; Chen, J. S.; Wu, H. B.; Wang, Z.; Lou, X. W. Quasiemulsion-Templated Formation of α-Fe2O3 Hollow Spheres with Enhanced Lithium Storage Properties. *J. Am. Chem. Soc.* **2011**, *133*, 17146-17148.

(22) Wang, Y.; Su, X.; Lu, S. Shape-Controlled Synthesis of TiO2 Hollow Structures and Their Application in Lithium Batteries. *J. Mater. Chem.* **2012**, *22*, 1969-1976.

(23) Cheng, H.; Huang, B.; Liu, Y.; Wang, Z.; Qin, X.; Zhang, X.; Dai, Y. An Anion Exchange Approach to Bi2WO6 Hollow Microspheres with Efficient Visible Light Photocatalytic Reduction of CO2 to Methanol. *Chem. Commun.* **2012**, *48*, 9729-9731.

(24) Zhu, J.; Ng, K. Y. S.; Deng, D. Hollow Cocoon-Like Hematite Mesoparticles of Nanoparticle Aggregates: Structural Evolution and Superior Performances in Lithium Ion Batteries. *ACS Appl. Mater. Interfaces* **2014**, *6*, 2996-3001.

(25) Cao, L.; Chen, D.; Caruso, R. A. Surface-Metastable Phase-Initiated Seeding and Ostwald Ripening: A Facile Fluorine-Free Process towards Spherical Fluffy Core/Shell, Yolk/Shell, and Hollow Anatase Nanostructures. *Angew. Chem. Int. Ed.* **2013**, *52*, 10986-10991.

(26) Addu, S. K.; Zhu, J.; Ng, K. Y. S.; Deng, D. A Family of Mesocubes. *Chem. Mater.* **2014**, *26*, 4472-4485.

(27) Zhao, J.; Zou, Y.; Zou, X.; Bai, T.; Liu, Y.; Gao, R.; Wang, D.; Li, G.-D. Self-Template Construction of Hollow Co3O4 Microspheres from Porous Ultrathin Nanosheets and Efficient Noble Metal-Free Water Oxidation Catalysts. *Nanoscale* **2014**, *6*, 7255-7262.

(28) Zhang, L.; Wu, H. B.; Lou, X. W. Metal–Organic-Frameworks-Derived General Formation of Hollow Structures with High Complexity. *J. Am. Chem. Soc.* **2013**, *135*, 10664-10672.

(29) Yang, H. G.; Zeng, H. C. Preparation of Hollow Anatase TiO2 Nanospheres via Ostwald Ripening. *J. Phys. Chem. B* **2004**, *108*, 3492-3495.

(30) Xin, G.-Q.; Ding, H.-P.; Yang, Y.-G.; Shen, S.-L.; Xiong, Z.-C.; Chen, X.; Hao, J.; Liu, H.-G. Triangular Single-Crystalline Nanorings of PbS Formed at the Air/Water Interface. *Cryst. Growth Des.* **2009**, *9*, 2008-2012.

(31) Zhu, J.; Ng, K. Y. S.; Deng, D. Micro Single Crystals of Hematite with Nearly 100% Exposed {104} Facets: Preferred Etching and Lithium Storage. *Cryst. Growth Des.* **2014**, *14*, 2811-2817.

(32) Hu, X.; Yu, J. C.; Gong, J.; Li, Q.; Li, G. α-Fe2O3 Nanorings Prepared by a Microwave-Assisted Hydrothermal Process and Their Sensing Properties. *Adv. Mater.* **2007**, *19*, 2324-2329.

(33) Tao, B.; Zhang, Q.; Liu, Z.; Geng, B. Cooperative Effect of pH Value and Anions on Single-Crystalline Hexagonal and Circular α-Fe2O3 Nanorings. *Mater. Chem. Phys.* **2012**, *136*, 604-612.

(34) Wang, Z.; Luan, D.; Madhavi, S.; Hu, Y.; Lou, X. W. Assembling Carbon-Coated α-Fe2O3 Hollow Nanohorns on the CNT Backbone for Superior Lithium Storage Capability. *Energy Environ. Sci.* **2012**, *5*, 5252-5256.

(35) Xu, X.; Cao, R.; Jeong, S.; Cho, J. Spindle-like Mesoporous α-Fe2O3 Anode Material Prepared from MOF Template for High-Rate Lithium Batteries. *Nano Lett.* **2012**, *12*, 4988-4991.

(36) Zhou, L.; Xu, H.; Zhang, H.; Yang, J.; B. Hartono, S.; Qian, K.; Zou, J.; Yu, C. Cheap and Scalable Synthesis of α-Fe2O3 Multi-Shelled Hollow Spheres as High-Performance Anode Materials for Lithium Ion Batteries. *Chem. Commun.* **2013**, *49*, 8695-8697.

(37) Wang, X.; Li, X.; Sun, X.; Li, F.; Liu, Q.; Wang, Q.; He, D. Nanostructured NiO Electrode for High Rate Li-Ion Batteries. *J. Mater. Chem.* **2011**, *21*, 3571-3573.

(38) Poizot, P.; Laruelle, S.; Grugeon, S.; Dupont, L.; Tarascon, J. M. Nano-Sized Transition-Metal Oxides as Negative-Electrode Materials for Lithium-Ion Batteries. *Nature* **2000**, *407*, 496-499.

(39) NuLi, Y.; Zeng, R.; Zhang, P.; Guo, Z.; Liu, H. Controlled Synthesis of α-Fe2O3 Nanostructures and Their Size-Dependent Electrochemical Properties for Lithium-Ion Batteries. *J. Power Sources* **2008**, *184*, 456-461.

(40) Cherian, C. T.; Sundaramurthy, J.; Kalaivani, M.; Ragupathy, P.; Kumar, P. S.; Thavasi, V.; Reddy, M. V.; Sow, C. H.; Mhaisalkar, S. G.; Ramakrishna, S.; Chowdari, B. V. R. Electrospun α-Fe2O3 Nanorods as a Stable, High Capacity Anode Material for Li-Ion Batteries. *J. Mater. Chem.* **2012**, *22*, 12198-12204.

(41) Reddy, M. V.; Yu, T.; Sow, C. H.; Shen, Z. X.; Lim, C. T.; Subba Rao, G. V.; Chowdari, B. V. R. α-Fe2O3 Nanoflakes as an Anode Material for Li-Ion Batteries. *Adv. Funct. Mater.* **2007**, *17*, 2792-2799.